



Synthesis of nano-NiXFe₂O₄ (X = Mg/Co) by citrate-gel method: structural, morphological and low-temperature magnetic properties

Abdul Gaffoor¹ · K. Chandra Babu Naidu² · D. Ravinder¹ · Khalid Mujasam Batoo³ · Syed Farooq Adil⁴ · Mujeeb Khan⁴

Received: 29 October 2019 / Accepted: 10 December 2019 / Published online: 16 December 2019
© Springer-Verlag GmbH Germany, part of Springer Nature 2019

Abstract

A series of Mg-doped NiFe₂O₄ (NMF) and Co-doped NiFe₂O₄ (NCF) nanoparticles were synthesized via citrate-gel method. The X-ray diffraction patterns of conventionally heated NMF and NCF nanoparticles confirmed the formation of single-phase cubic spinel structures. Further, the variation of structural parameters as a function of compositions was described. The morphology of NMF and NCF materials was investigated using scanning and transmission electron microscopes (SEM and TEM). In addition, the formation of tetrahedral (A-site) and octahedral (B-site) locations of NMF and NCF was obtained from the Fourier transform infrared spectra (FTIR). Furthermore, the room- and low-temperature magnetic properties were studied for NMF and NCF nanoparticles using magnetization versus magnetic field (M-H) loops and zero field cooled (ZFC) and field cooled (FC) curves, respectively. The results revealed that NMF and NCF nanoparticles exhibited superparamagnetic (SPM) nature at room temperature.

1 Introduction

In general, ferrite nanoparticles are the class of magnetic nanoparticles which acquired significant attention in different scientific, medical and industrial fields owing to their electrical, magnetic, and optical properties [1]. These ferrite nanoparticles are normally the metal oxides having the general chemical formula of AB₂O₄, where 'A' tends to divalent elements such as Ni, Mg, Zn, Mn, Co, Cu and Fe, and 'B' is associated with the trivalent Fe element [2]. Thus, the above chemical formula can be written as AFe₂O₄. Moreover, the ferrites showed variety of applications to the scientific community, viz., waste water treatment, drug delivery system, magnetic resonance imaging (MRI), transformer and inductor core devices, photocatalysis, magnetic tapes, magnetic

recording media, magnetic memory devices, multilayer chip inductors (MLCI), electromagnetic shields, soft magnets fabrication, microwave absorbers, antenna devices, magneto-hyperthermia treatment, superparamagnetism, green anodes, magnetic refrigeration, magneto-optical devices, spintronics, sensors, etc., [1–9].

However, it was an observed fact that many researchers synthesized magnetic nanoparticles such as NiFe₂O₄, MgFe₂O₄, and CoFe₂O₄ via different preparation techniques and further investigated the structural, morphological, electrical, magnetic (M–H loops), superparamagnetic, piezoelectric, and optical properties [10–17]. In addition, some other scientists focussed on doping various elements to the above-said parent materials to enhance the electrical and magnetic properties for the required applications. In view of this, NiMg ferrites, LiNi ferrites, NiCuZn ferrites, Co-based ferrites, rare earth-based spinel ferrites [18–25] etc., were studied for electrical and magnetic properties. Nevertheless, these properties were confined to room (RT) or high temperatures. In particular, the electrical properties were measured from RT to high temperatures for finding the Curie transition temperatures (T_c). On the other hand, the magnetic properties such as magnetic permeability (RT to beyond T_c) [18, 19] and magnetic hysteresis (M–H) loops at RT [18–25] were recorded. These results provided the advancement of magnetic moment of parent materials. As a whole, it can

✉ D. Ravinder
ravindergupta28@rediffmail.com

¹ Department of Physics, Osmania University, Hyderabad, Telangana 500007, India

² Dept. of Physics, GITAM Deemed To Be University, Bangalore, Karnataka 562163, India

³ King Abdullah Institute For Nanotechnology, King Saud University, P.O. Box 2455, Riyadh 11451, Saudi Arabia

⁴ Department of Chemistry, College of Science, King Saud University, P.O. Box 2455, Riyadh 11451, Saudi Arabia

be understood that there were no reports available on low-temperature magnetic properties of Mg/Co-doped NiFe_2O_4 nanoparticles using ZFC and FC curves for evaluating the SPM nature. In this context, the authors interested to explore the low-temperature magnetic properties of Mg/Co-doped NiFe_2O_4 nanoparticles using M–H loops and ZFC and FC curves via citrate-gel method.

2 Experimental method

2.1 Preparation of NMF and NCF nanoferrites

For the synthesis of NMF nanoparticles, $\text{Ni}(\text{NO}_3)_2 \cdot 6\text{H}_2\text{O}$, $\text{Fe}(\text{NO}_3)_3 \cdot 9\text{H}_2\text{O}$, and $\text{Mg}(\text{NO}_3)_2 \cdot 6\text{H}_2\text{O}$ (each of 99.9% purity, Sigma-Aldrich) were chosen as precursors in nitrate form. Further, these raw materials were dissolved in deionized water by considering 1:3 ratios. In next step, the citric acid (chelating agent) was added to the nitrate mixture solution to prepare the aqueous solution. The resultant solution was poured in a fresh beaker and further, it was stirred constantly using magnetic stirrer to obtain homogeneous mixture. Later, the above solution was mixed with NH_3 solution to keep the pH identical to 7. The resultant solution at this stage was heated up to 100°C on the hot plate of magnetic stirrer. Thus, after some time, the gel-like material called the citrate precursor was formed during the evaporation process. Again, this citrate precursor was heated at $180\text{--}200^\circ\text{C}$. At this stage, the water content and few gaseous products were eliminated from the resultant gel material. In the mean time, the autocombustion reaction took place. This was just like volcanic eruption and the final material was produced in dark gray color with elongated asymmetric fiber type of shape. Furthermore, the prepared materials were removed and ground as well in the agate mortars to achieve a fine powder. This powder was once again calcined at 500°C in a conventional furnace for 4 h to form a spinel structured material. The photographs containing the three main steps in citrate-gel autocombustion technique are shown in Fig. 1. The similar method and steps were followed for the preparation of $\text{Ni}_{1-x}\text{Co}_x\text{Fe}_2\text{O}_4$ ($x=0.0\text{--}1$) nanoferrites as

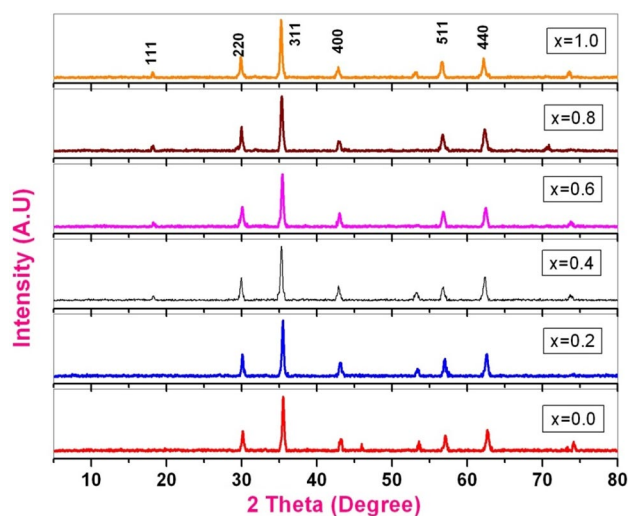


Fig. 2 XRD patterns of Ni–Mg nanoferrites calcined at 500°C

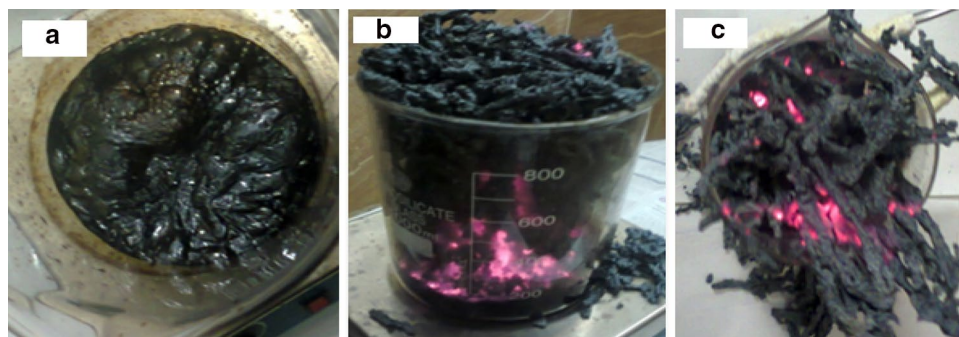
in the case of $\text{Ni}_{1-x}\text{Mg}_x\text{Fe}_2\text{O}_4$ ($x=0.0\text{--}1$). Specifically, the $\text{Mg}(\text{NO}_3)_2 \cdot 6\text{H}_2\text{O}$ was replaced by $\text{Co}(\text{NO}_3)_2 \cdot 6\text{H}_2\text{O}$ (99.9% purity, Sigma-Aldrich). Afterwards, the materials were analyzed using the X-ray diffractometer (Bruker XRD, $\text{Cu}_{K\alpha}$, $\lambda=0.15406\text{ nm}$), High-Resolution Transmission Electron Microscope (HRTEM: Model Tecnai G20, FEI, USA), Scanning Electron Microscope (Ultra 55 SEM Carl Zeiss), FT-IR spectrophotometer (IR affinity-1, Shimadzu) and Vibrating Sample Magnetometer (EV-7 VSM with Max. applied field $\pm 15\text{ kOe}$) for discussing the structural, morphological, functional groups and low-temperature magnetic properties, respectively.

3 Results and discussion

3.1 X-ray diffraction analysis of $\text{Ni}_{1-x}\text{Mg}_x\text{Fe}_2\text{O}_4$ nanoparticles

The diffraction patterns of conventionally heated (at 500°C) $\text{Ni}_{1-x}\text{Mg}_x\text{Fe}_2\text{O}_4$ ($x=0.0\text{--}1$) nanoparticles are shown in Fig. 2. The reflection planes were indexed using the Miller indices

Fig. 1 a Gel formation, b combustion method and c gray-colored product



of (111), (220), (311), (400), (511) and (440) which in turn indicated the existence of single-phase cubic spinel structure. This confirmed that the prepared samples were of high phase purity in nature. These were consistent with the standard JCPDS: 71-1232. In addition, it was noted that the maximum intensity was noted in the (311) plane. From the diffraction patterns, it was clear that the cubic single phases were formed. Besides, the broad width of the peaks in the NMF materials revealed the small-sized nanoparticles. However, in case of the heated NMF samples, the cubic spinel structure remained the same. The average crystallite size was calculated for all heated NMF samples using Scherrer's equation as mentioned in reference [26]. Specifically, this formula was applied to each diffraction peak of NMF (as indexed in Fig. 2). As a result, many crystallite size values were noted and further, the average crystallite size was evaluated. Hence, this can provide more reliability in achieving the average crystallite size. The obtained results (average crystallite size values) are reported in Table 1. It can be obviously seen from Table 1 that the heated NMF materials revealed the presence of sharp and narrow peaks. This evidenced that the heated samples expressed the high crystallinity in nature. The average crystallite size of the sintered samples was found to be in the range of 13.8–29.6 nm (shown in Table 1) for different compositions. The high microstrain produced during the reaction can be responsible for this behavior of acquiring low crystallite size values for all compositions [23]. According to literature survey, no other method showed the Ni–Mg ferrites with such a small average crystallite size except the citrate-gel autocombustion method [23, 24]. Normally, the conventional methods can consume very high temperatures and prolonged heating time [24, 27]. The structural parameters such as lattice constant ($a = d(h^2 + k^2 + l^2)^{1/2}$, where d is the inter-planar spacing and (hkl) are the Miller indices), X-ray density [$D_x = ZM/Na^3$, where 'Z' is the no. of molecules per unit cell ($Z = 8$), 'M' is the molecular weight of the composition, 'N' is Avogadro's number (6.023×10^{23}) and 'a' is the lattice parameter] and volume of the unit cell ($V = a^3$) of the individual composition were calculated and results are tabulated in Table 1.

The data presented in Table 1 show the variation trend of different structural parameters as a function of Mg content. In this concern, the lattice parameter was noted to be increasing with an increase in Mg content and, therefore, it obeyed Vegard's law [28]. This kind of manner can be well understood by means of ionic radii of nickel and magnesium cations. As per the Shannon ionic radii table [29], the Mg⁺² cations will have the octahedral ionic radius of 0.72 Å which is larger in value than the octahedral ionic radius of 0.69 Å of Ni⁺² ions. Thus, as the number of Mg cations is increased, the Mg⁺² ions will preferably occupy the Ni⁺²-sites. Thus, the nickel cations of smaller ionic radii will be replaced by the magnesium cations of larger ionic radii. As a result, the volume of unit cell was increased which led to the enhancement of unit cell dimensions. Apart from these, the behavior of X-ray density (D_x) was seen with increase in 'x' value. In general, the theoretical (X-ray) density is a dependent parameter of molecular weight of compositions. It was observed that the molecular weight of NMF materials was decreasing with 'x' value. Consequently, the theoretical density was also decreased from 5.362 to 4.530 g/c.c., as a function of composition. These kinds of reports were seen earlier in the literature [30–32]. In addition, the density and atomic concentration of magnesium and nickel were noted to be 1.748 g/c.c., 8.905 g/c.c and $4.3 \times 10^{22} \text{ cm}^{-3}$, $9.1 \times 10^{22} \text{ cm}^{-3}$, respectively [18]. The increase of lattice constant from 8.342 to 8.372 Å for $x = 0.0$ – 1.0 contents was also one of the reasons for the decrease of the X-ray density. Moreover, the unit cell volume was observed to be increasing with increase in 'x' due to increase of lattice constants. Finally, the distance between magnetic ions (hopping length) in A site (tetrahedral) ($d_A = 0.25a\sqrt{3}$) and B site (octahedral) ($d_B = 0.25a\sqrt{2}$) was calculated (where the symbols have their usual meaning) [23, 24] and is listed in Table 1 as a function 'x'.

3.2 X-ray diffraction analysis of Ni_{1-x}Co_xFe₂O₄ nanoferrites

The XRD patterns of heated NCF nanoparticles are depicted in Fig. 3. The crystalline phases were identified and

Table 1 Values of molecular weight, lattice parameter (a), X-ray density (D_x), volume of the unit cell (V) and wavenumbers of A and B sites of Ni_{1-x}Mg_xFe₂O₄ ferrites

x	Average crystallite size (nm)	Lattice parameter (Å)	Unit cell volume (Å) ³	X-ray density (gm/cc)	A-site d_A (Å)	B-site d_B (Å)	ν_1 (cm ⁻¹)	ν_2 (cm ⁻¹)
0.0	29.55	8.342	580.511	5.362	3.6122	2.9494	606.57	495.29
0.2	26.71	8.348	581.764	5.212	3.6127	2.9497	617.602	483.59
0.4	25.94	8.354	583.019	5.039	3.6142	2.9510	617.82	485.41
0.6	23.81	8.360	584.277	4.869	3.6175	2.9537	617.85	482.99
0.8	18.46	8.366	585.535	4.692	3.6226	2.9578	616.24	483.60
1	13.82	8.372	586.796	4.530	3.6242	2.9590	617.01	484.60

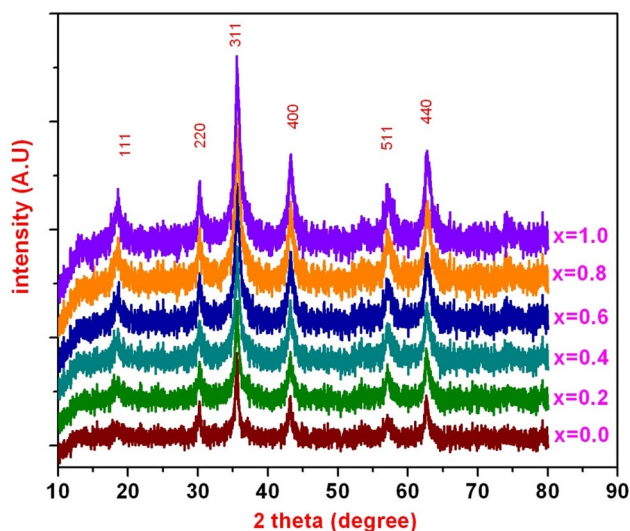


Fig. 3 XRD patterns of Ni–Co ferrites calcined at 500 °C

compared with the standard JCPDS: 22-1086. This comparison evidenced that upon doping with the cobalt cations, the nickel ferrite showed the single-phase cubic spinel structure. The diffraction peaks were indexed using Miller indices as shown in Fig. 3. Similar crystallinity and diffraction peak width were observed for both NCF and NMF nanoparticles. The average crystallite size was calculated from all the diffraction peaks and is listed in Table 2. From Table 2, it was clear that nanosized Ni–Co ferrite powders can be directly synthesized by citrate-gel autocombustion method. The formed sharper and narrow peaks after calcination indicated the improvement of crystallinity. The measured average crystallite size from all the diffraction peaks of various NCF compositions was in the range of 16.4–32.1 nm (shown in Table 2). This kind of low crystallite size values can be normally attributed to the high magnitude of microstrain developed during the reaction process [23]. It was clear that the citrate-gel method can only result in obtaining such small average crystallite size of Ni–Co ferrites. In the literature, the small crystallite size was obtained for different ferrite

materials using the present synthesis method [23, 24]. The structural parameters such as lattice constant (a), X-ray density (D_x) and volume of the unit cell of the individual composition were calculated and results are listed in Table 2. The lattice constants were found to be increasing from 8.342 to 8.362 Å with increase of Co^{+2} cations in the nickel ferrite system. The variation trend of lattice constants of NCF can be elucidated by means of ionic radii of the cations. It was known that the octahedral ionic radius of cobalt cations is ~ 0.82 Å which is larger than the octahedral ionic radius of nickel cations (0.78 Å). Therefore, if the cobalt cations are doped to the nickel ferrite system, the cobalt cations of high ionic radii can replace the nickel ions of small ionic radii. The X-ray density was noted to be decreasing from 5.363 to 5.328 g/c.c., with increase of cobalt content in the nickel ferrite–spinel ferrite system. It had happened due to the decrease of molecular weight as a function of composition. In addition, the density and atomic concentration of cobalt and nickel were noted to be 8.863 g/c.c, 8.905 g/c.c and $8.933 \times 10^{22} \text{ cm}^{-3}$, $9.1 \times 10^{22} \text{ cm}^{-3}$, respectively. This reinforced the decreasing trend of the resultant X-ray density. Besides, the increase of lattice constant from 8.342 to 8.362 Å for $x=0.0$ to 1.0 contents was also one of the reasons for the decrease of the X-ray density. In addition, the distance between magnetic ions (hopping length) in A site (tetrahedral) ($d_A = 0.25a\sqrt{3}$) and B site (octahedral) ($d_B = 0.25a\sqrt{2}$) of NCF was calculated (where the symbols have their usual meaning) [23, 24] and is listed in Table 2 as a function ‘ x ’. It was observed that the hopping length was increased with increase of the Co content nickel ferrite system.

3.3 SEM and TEM analyses

The SEM images of NMF samples are shown in Fig. 4. It was obviously noticed that the surface morphology of all samples revealed the identical grains in shape. Besides, the well-defined and agglomerated grains were seen. This type of agglomeration among the nanosized grains was attributed to the existence of the proportional relationship between

Table 2 Values of molecular weight, lattice parameter (a), X-ray density (D_x), volume of the unit cell (V) and wave numbers of A and B sites of $\text{Ni}_{1-x}\text{Co}_x\text{Fe}_2\text{O}_4$ ferrites

x	Average crystallite size (nm)	Lattice parameter (Å)	Unit cell volume (Å) ³	X-ray density (gm/cc)	A site d_A (Å)	B site d_B (Å)	ν_1 (cm ⁻¹)	ν_2 (cm ⁻¹)
0.0	32.11	8.342	580.511	5.363	3.612	2.949	606.57	495.29
0.2	29.03	8.346	581.346	5.356	3.613	2.950	609.1	497.29
0.4	24.80	8.350	582.182	5.349	3.615	2.952	606.59	494.76
0.6	23.44	8.354	583.019	5.343	3.617	2.953	607.77	496.09
0.8	18.05	8.358	583.857	5.336	3.619	2.954	610.71	497.69
1	16.40	8.362	584.696	5.328	3.620	2.956	609.51	495.69

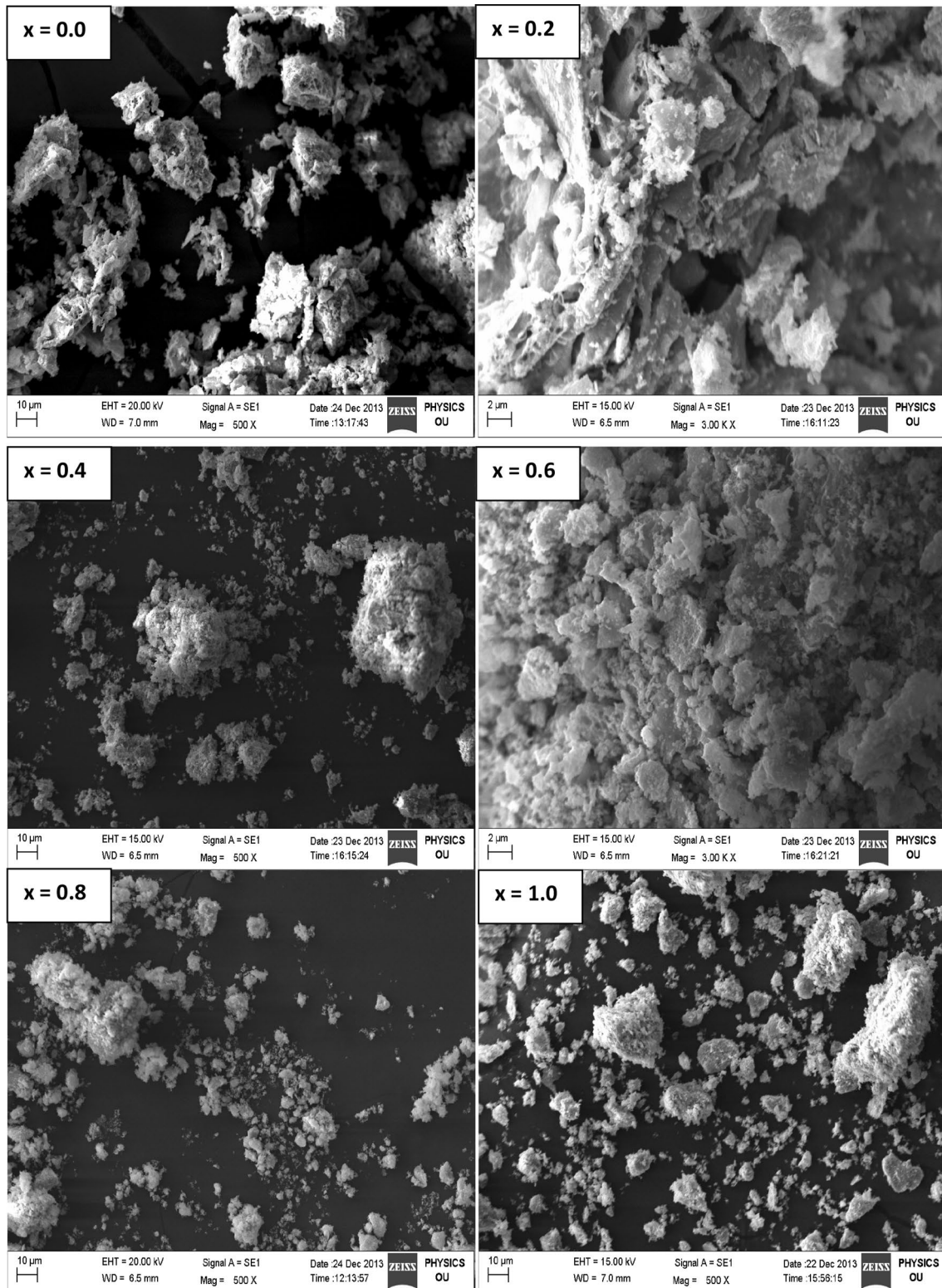


Fig. 4 SEM images of Ni_{1-x}Mg_xFe₂O₄ nanoferrites

the permanent magnetic moment and volume of grain [33]. Moreover, the heating resulted to form solid bodies from

the well-faceted grains. It was observed due to the porous network of sintered bodies. In addition, an enlarged mass of

compound formation was observed due to the influence of magnesium ions. The SEM micrographs also indicated that the grain size of the sample was in the nanometer region. The TEM was performed for all the samples of Ni–Mg nanoferrites at 20 nm scale bar which is shown Fig. 5. The TEM results indicated the presence of nanoparticles having the size less than 20 nm for all samples, that is, the particle size was observed to be changing from 14.8 to 18.3 nm for all contents. The particles were seemed to be round in shape which formed loose aggregates. The presence of various compositional elements of NMF materials was examined by energy-dispersive spectra (EDS) including the At % (atomic) and Wt % (weight). These are presented in Table 3. The

EDS of various compositions of NMF are shown in Fig. 6. The compounds revealed the presence of Ni, Mg, Fe and O without precipitating cations.

The SEM micrographs of NCF nanoparticles are presented in Fig. 7. It was clear from Fig. 7 that the NCF samples showed the presence of the homogeneous grains comprising of agglomeration in nature. This was confirmed by aggregation of grains found in nanometric region. In addition, the uniform nature of grains was evidenced from the good crystalline nature of NCF in the case of XRD patterns. It was a well familiar fact that there may be a favorable case of producing the iron oxide during the preparation of NCF and hence the pores will be developed. This kind

Fig. 5 TEM images of $\text{Ni}_{1-x}\text{Mg}_x\text{Fe}_2\text{O}_4$ ($X=0.0-1.0$)

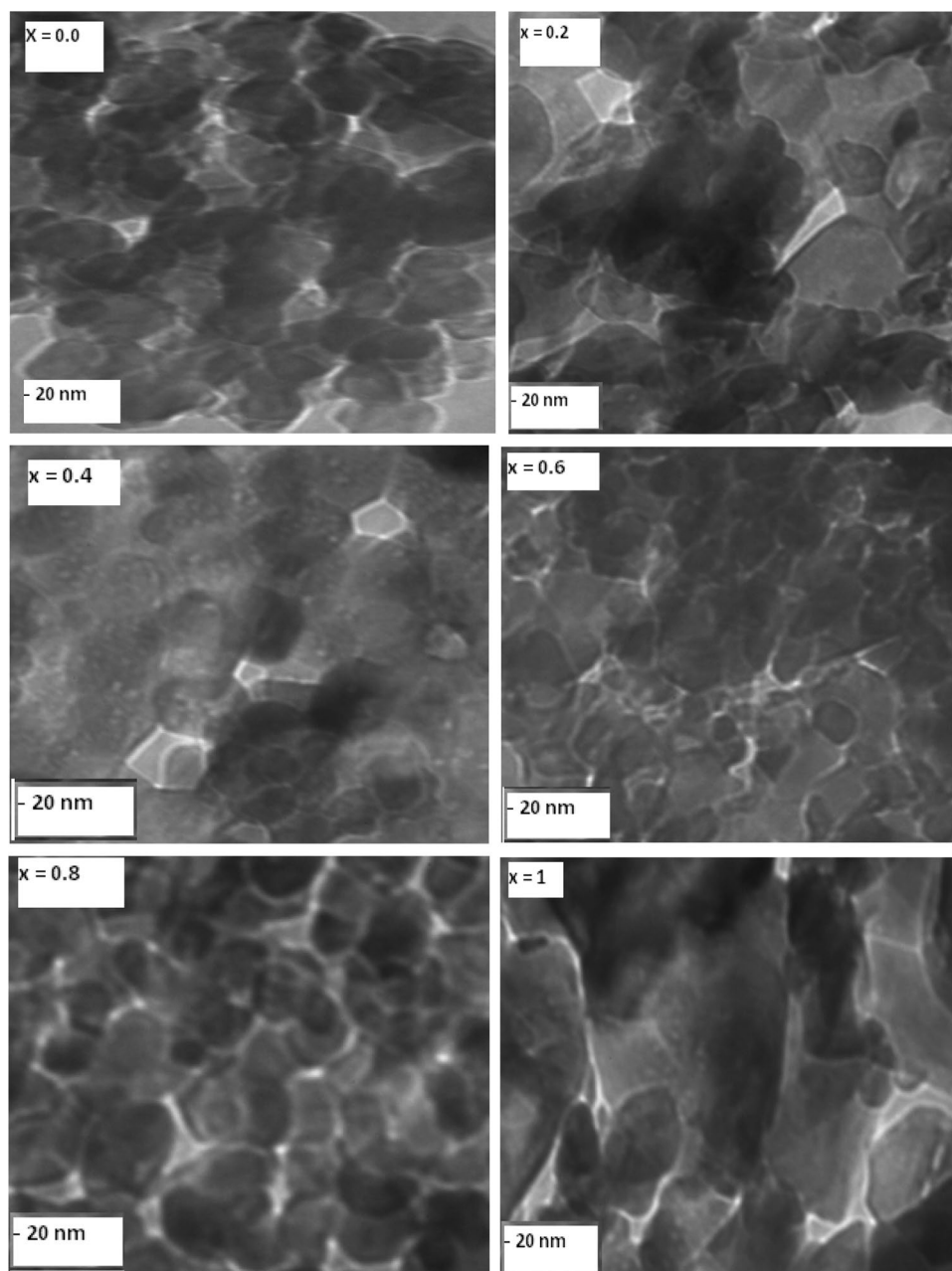
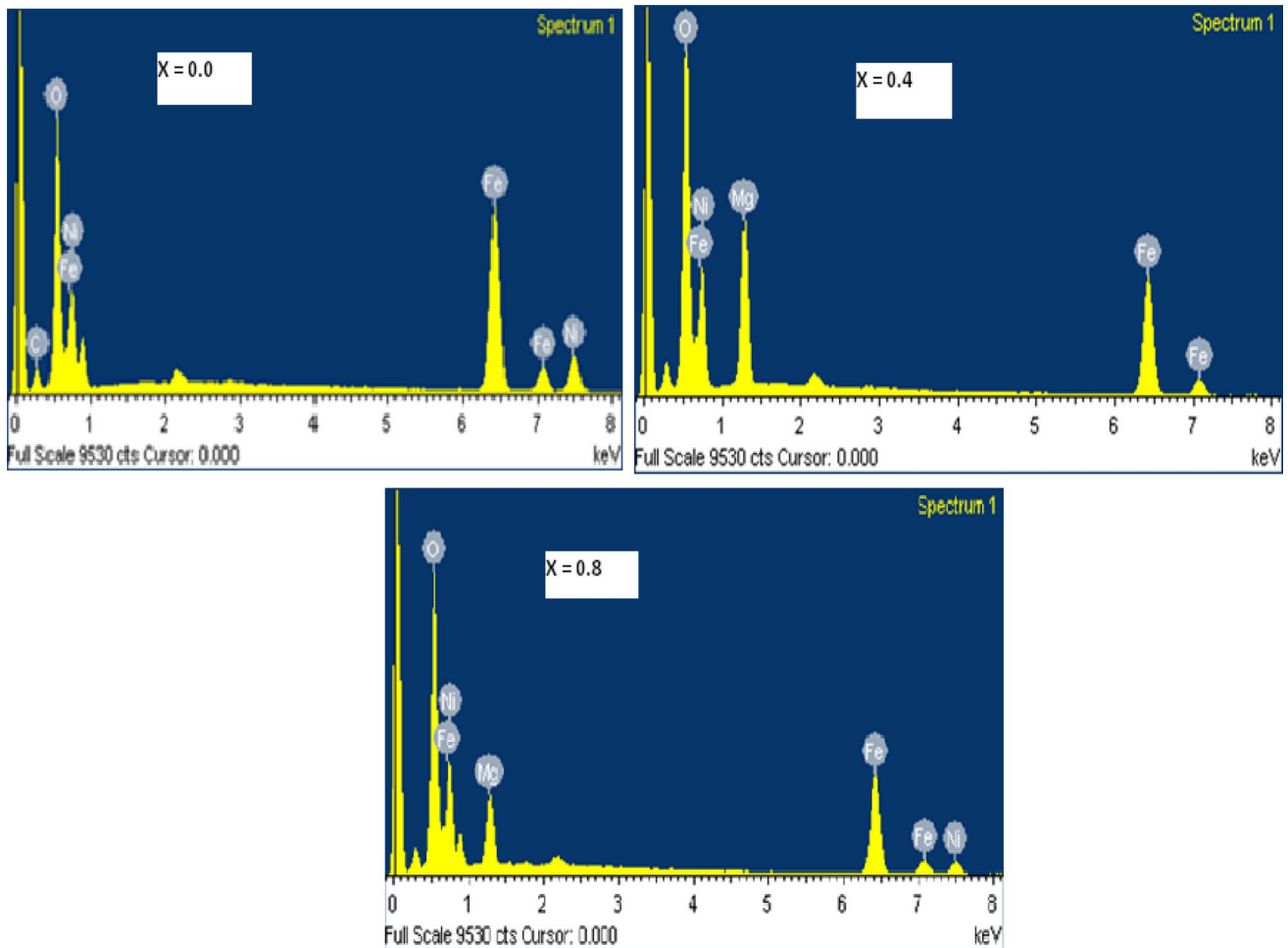


Table 3 Elements of each content of Ni–Mg ferrites analyzed by % weight obtained by EDS

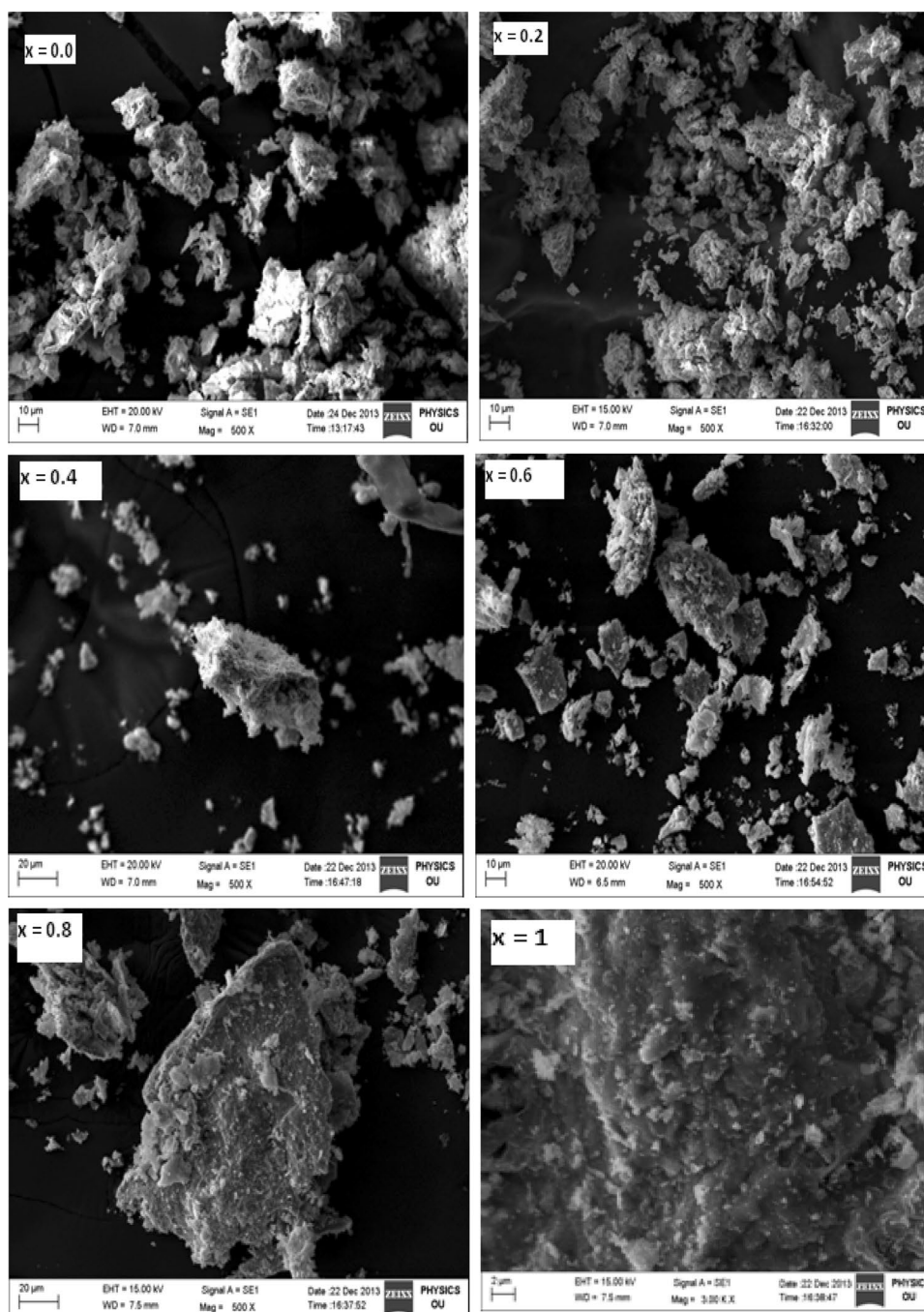
Element sample	O		Ni		Mg		Fe	
	Wt%	At%	Wt%	At%	Wt%	At%	Wt%	At%
NiFe ₂ O ₄	29.93	61.88	18.12	9.50	0.0	0.0	51.92	28.62
Ni _{0.8} Mg _{0.2} Fe ₂ O ₄	30.72	59.09	15.83	8.28	4.55	5.75	48.85	26.87
Ni _{0.6} Mg _{0.4} Fe ₂ O ₄	37.56	67.20	15.32	7.47	1.78	2.10	45.33	23.23
Ni _{0.4} Mg _{0.6} Fe ₂ O ₄	36.25	63.51	9.15	4.37	7.25	8.35	47.35	23.77
Ni _{0.2} Mg _{0.8} Fe ₂ O ₄	29.36	55.78	5.80	3.00	8.39	10.50	56.45	30.72
MgFe ₂ O ₄	38.37	62.91	0.0	0.0	13.37	14.42	48.38	22.72


Fig. 6 EDS images of Ni_{1-x}Mg_xFe₂O₄ nanoferrites

of pore development can be almost removed by means of sintering process which can normally enhance the grain growth. This had happened in the morphology of NCF materials. It was also noticed that the agglomeration was increased upon increasing the cobalt content. Moreover, the apparent grain size was noted to be increasing with composition as it was evidenced in case of X-ray diffraction patterns of NCF. The TEM photographs of NCF were

extracted at 20 nm scale bar and are shown in Fig. 8. The morphology suggested that the particles were round in shape and weak aggregates. The average particle size was observed to be altering from 13.6 to 19.4 nm. The existence of Ni, Co, Fe and O elements was confirmed using the EDS of NCF. The EDS photos of NCF materials are shown in Fig. 9. Besides, the atomic and weight percentages of elements are shown in Table 4.

Fig. 7 SEM images of $\text{Ni}_{1-x}\text{Co}_x\text{Fe}_2\text{O}_4$ with $x=0.0-1.0$

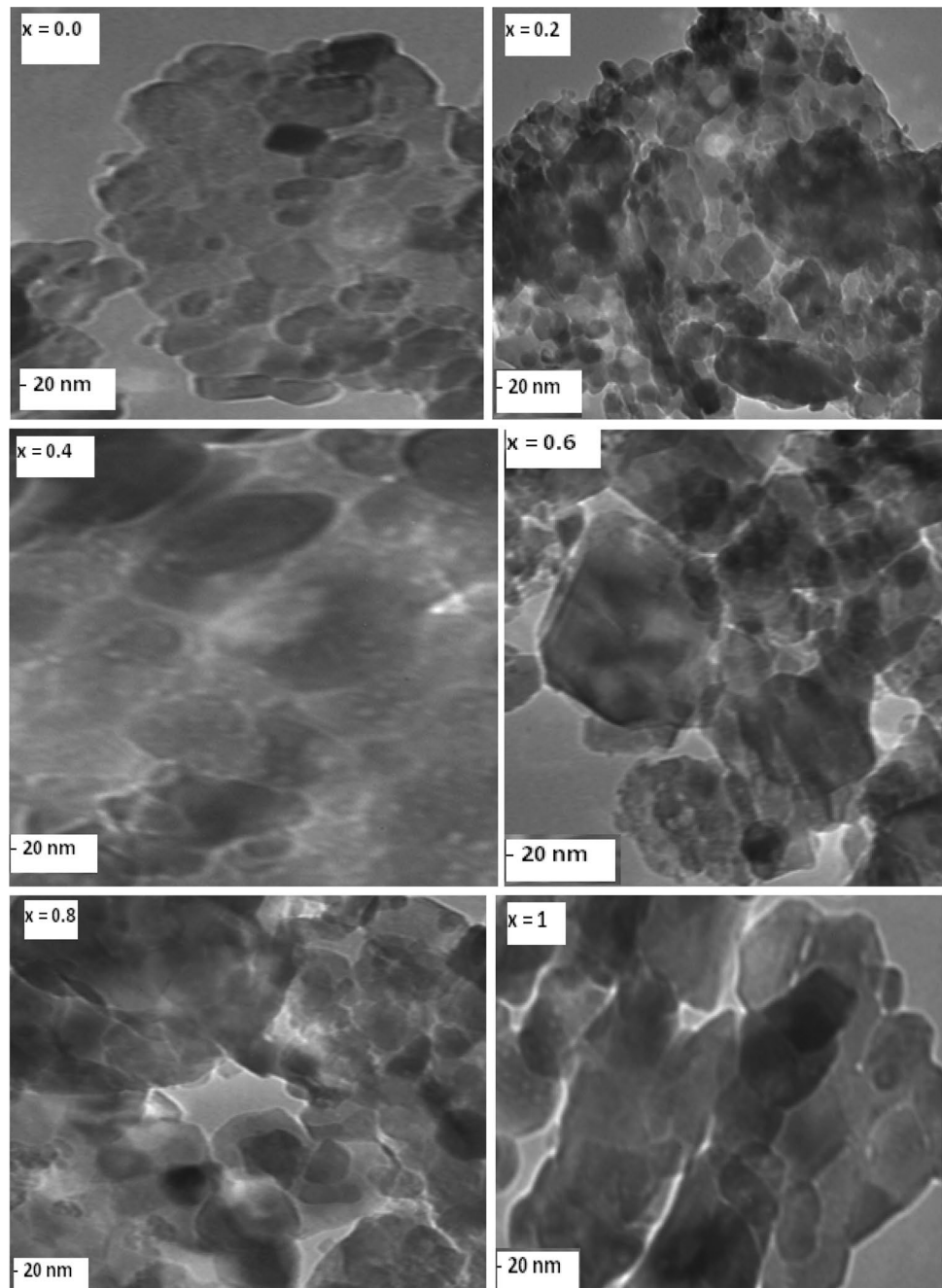


3.4 FTIR spectral analysis

The FTIR spectra of NMF samples are recorded over the range of $200-800\text{ cm}^{-1}$ as depicted in Fig. 10. In general, the FTIR spectra of NMF were used to indicate the tetrahedral and octahedral positions of cubic spinel structure (Table 1). In the current investigation, the absorption bands ν_1 (high frequency) and ν_2 (low frequency) were noticed at $\sim 600\text{ cm}^{-1}$ and $\sim 400\text{ cm}^{-1}$. Thus, it exhibited the evolution of cubic spinel structure without

any impurity by containing two sub-lattices of A and B [34, 35]. The ν_1 was varying over the frequency of $606-618\text{ cm}^{-1}$ while ν_2 was noted to be altering from 483 to 496 cm^{-1} . Therefore, it was confirmed that there was a difference between tetrahedral and octahedral positions. This can be attributed to the distance between ferric and oxygen ions at A and B sites. Similar observation was seen in the FTIR spectral analysis for the Ni-Mg ferrite system reported by previous scientists [36, 37], the FTIR spectra of spinels showed ν_1 at $\sim 600\text{ cm}^{-1}$ which was assigned to

Fig. 8 TEM images of Ni_{1-x}Co_xFe₂O₄ (x = 0.0–1.0)



the A site. On the other hand, ν_2 observed at $\sim 400\text{ cm}^{-1}$ was associated with the B site. Indeed, it was found that the addition of magnesium supported in broadening the absorption band at around 484 cm^{-1} . This became more prominent at high concentration of Mg cations. It was seen that the positions of the absorption bands were composition dependent which may be due to the cation–oxygen bond distances. Likewise, the FTIR spectra of NCF nanoparticles were recorded over $200\text{--}800\text{ cm}^{-1}$ wavenumber range as shown in Fig. 11. The ν_1 and ν_2 were assigned to A and B sites at around 600 and 400 cm^{-1} , respectively.

These absorption bands for different compositions are listed in Table 2. It was evidently seen that ν_1 was changed from 606 to 610 cm^{-1} . On the other hand, ν_2 was observed to be changing from 494 to 497 cm^{-1} .

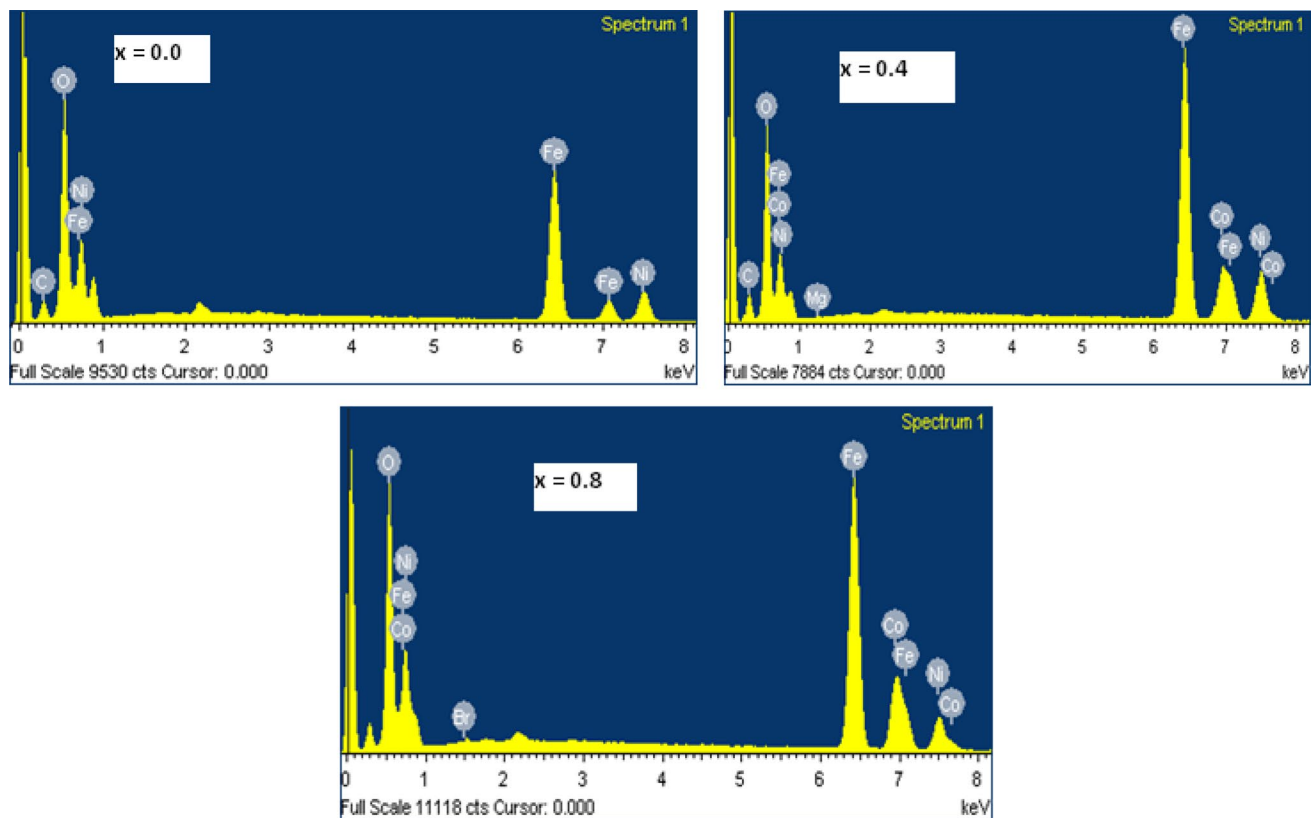


Fig. 9 EDS images of $\text{Ni}_{1-x}\text{Co}_x\text{Fe}_2\text{O}_4$ nanoferrites

Table 4 Elements of each sample composition analyzed by %weight obtained by EDS

Element composition	O		Ni		Co		Fe	
	Wt%	At%	Wt%	At%	Wt%	At%	Wt%	At%
NiFe_2O_4	29.93	61.88	18.12	9.50	0.0	0.0	51.92	28.62
$\text{Ni}_{0.8}\text{Co}_{0.2}\text{Fe}_2\text{O}_4$	21.85	49.77	19.31	12.00	6.00	3.71	52.83	34.52
$\text{Ni}_{0.6}\text{Co}_{0.4}\text{Fe}_2\text{O}_4$	28.97	59.23	9.11	5.07	14.91	8.28	46.35	27.15
$\text{Ni}_{0.4}\text{Co}_{0.6}\text{Fe}_2\text{O}_4$	33.38	42.77	12.15	5.70	9.18	4.29	45.28	41.24
$\text{Ni}_{0.2}\text{Co}_{0.8}\text{Fe}_2\text{O}_4$	33.53	51.63	2.69	0.91	11.26	3.80	52.50	43.66
CoFe_2O_4	34.56	66.10	0.0	0.0	10.88	9.50	46.62	24.34

3.5 Magnetic properties of $\text{Ni}_{1-x}\text{Mg}_x\text{Fe}_2\text{O}_4$ nanoferrite system

3.5.1 Room temperature magnetization measurements using VSM

Figure 12 revealed the M–H loops (hysteresis loop) of NMF materials heated at 500 °C. The different magnetic parameters, viz., saturation magnetization— M_s , remanence magnetization— M_r , coercivity— H_c , and squareness ratio (M_r/M_s), were measured. The results are listed in Tables 5 and 6. From Fig. 12 and Table 5, it was obvious that both saturation magnetization and coercivity were decreased with increase of Mg content. In general, the magnetic properties of soft

ferrites will be affected due to the concentration of dopant, type of dopant and morphology of the samples. However, the microstructure showed strong influence on the variation of magnetic parameters. In view of this, it was noted that the larger is the grain size, the higher is the saturation magnetization [18, 19]. From Table 5, it was observed that NiFe_2O_4 ferrites exhibited large grain size and hence high saturation magnetization and coercivity can be observed as depicted from hysteresis loop (Fig. 12). With increase in Mg content, the grain size was decreased and, therefore, the M_s values were also decreased. The M_s value (at room temperature) was decreased from 17.26 to 10.50 emu/g due to the doping of Mg ions in NMF system. This type of reduction of M_s value can be described owing to the fact

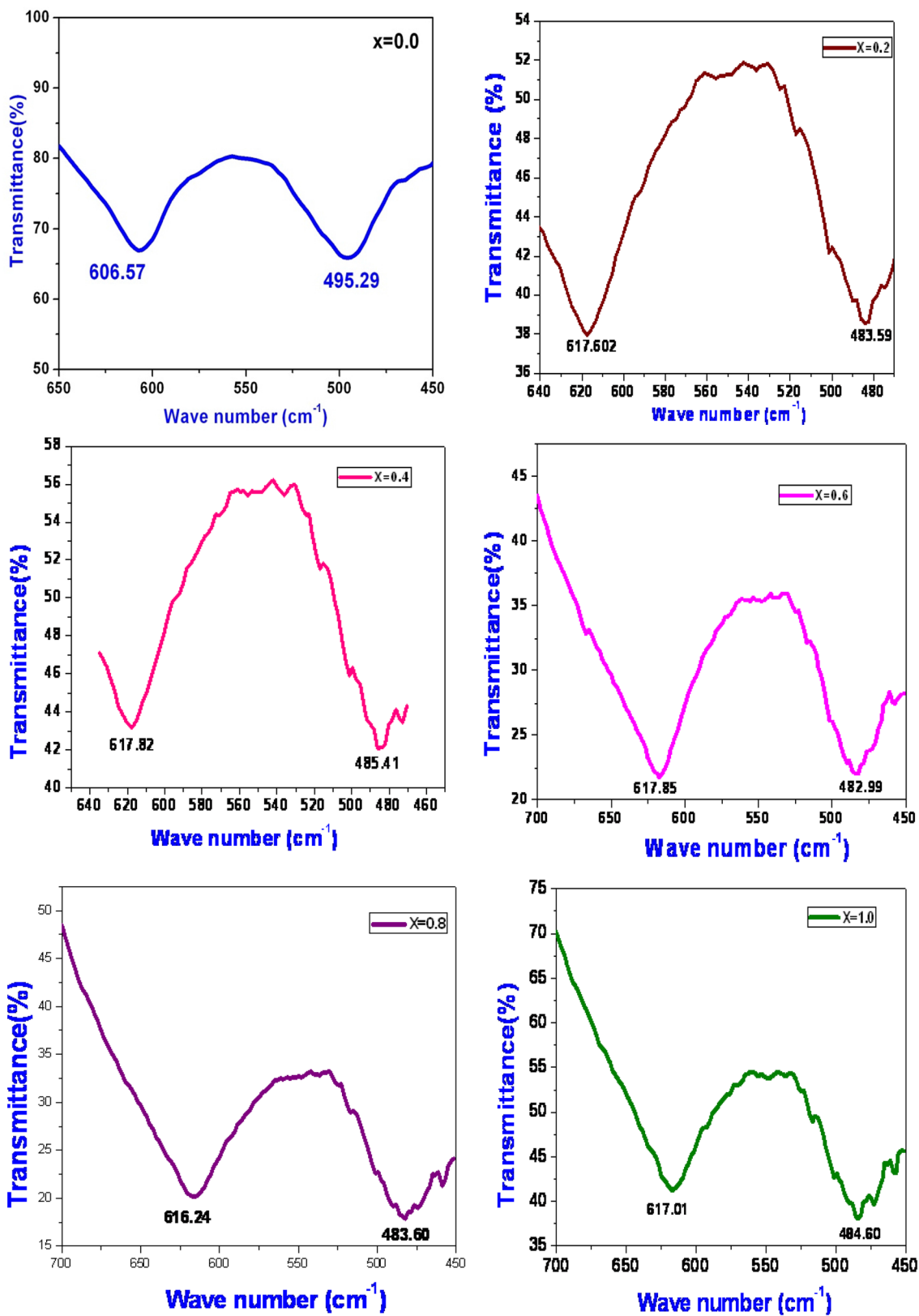


Fig. 10 FTIR spectra of Ni_{1-x}Mg_xFe₂O₄ nano-ferrites with (x = 0.0–1.0)

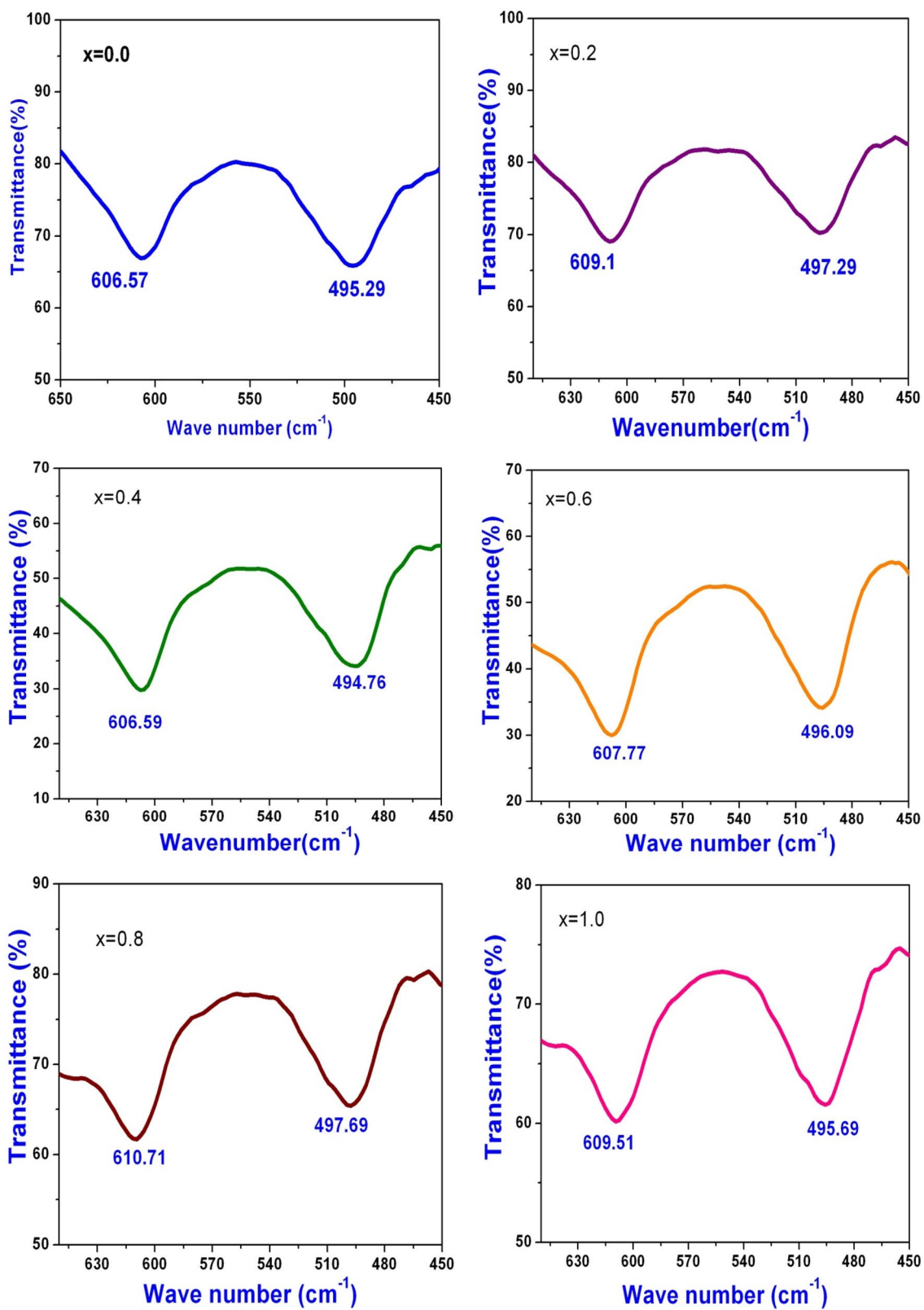


Fig. 11 FTIR patterns of Ni_{1-x}Co_xFe₂O₄ nanoferrites

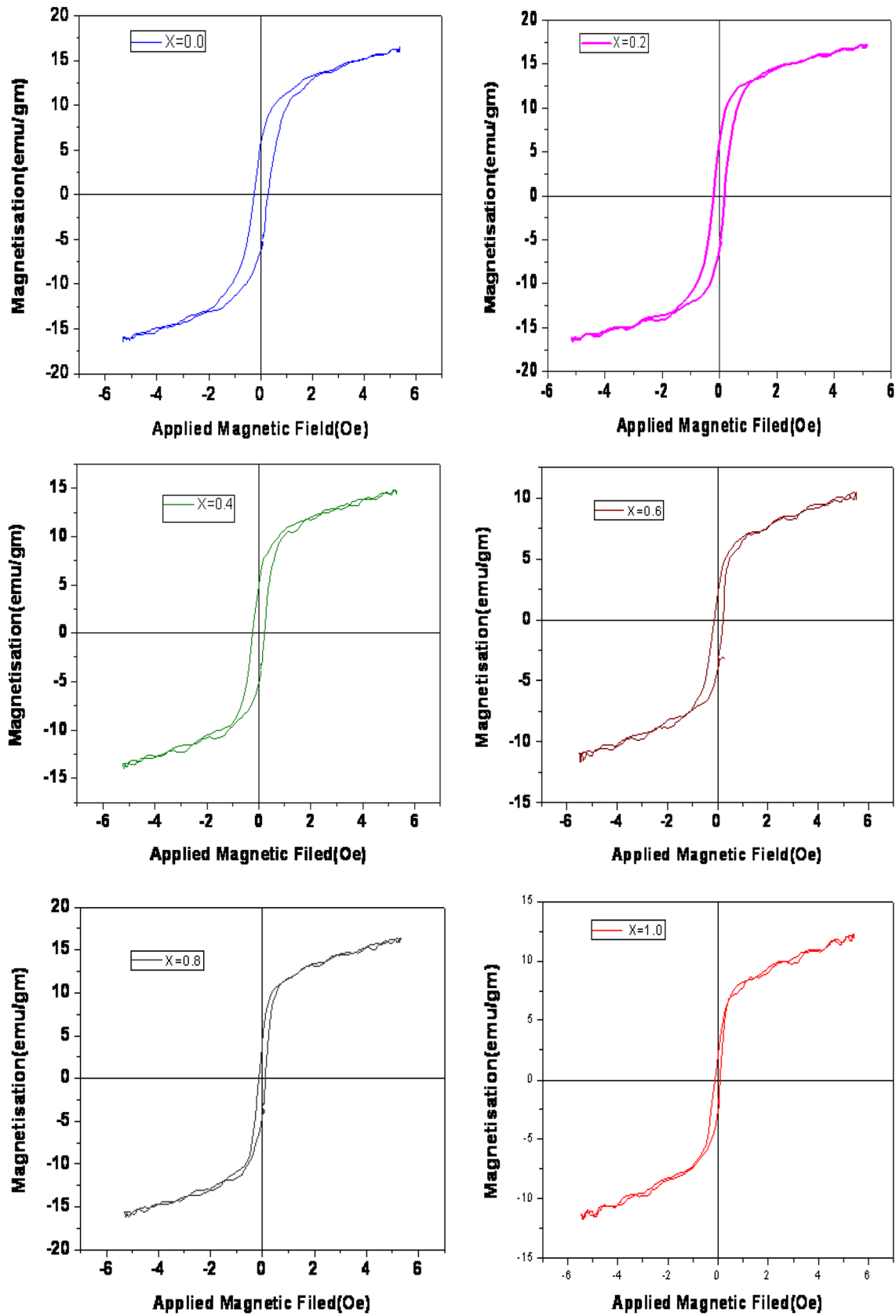


Fig. 12 M–H loops for NiMg ferrite nanomaterials

Table 5 Magnetic parameters of $\text{Ni}_{1-x}\text{Mg}_x\text{Fe}_2\text{O}_4$ ($x=0.0-1.0$) from hysteresis loops

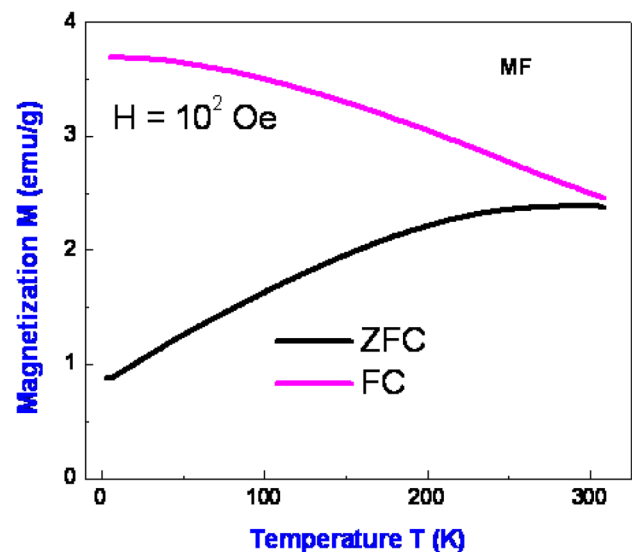
x	M_s (emu/g)	M_r (emu/g)	H_c (Oe)	M_r/M_s	K (erg/Oe)	Magnetic moment ($\mu_B/\text{f.u.}$)
0.0	17.27	7.62	273.78	0.44	4823.61	0.72
0.2	16.45	6.53	224.40	0.39	3766.66	0.67
0.4	16.43	6.24	193.23	0.37	3238.83	0.64
0.6	14.84	4.61	175.10	0.31	2652.46	0.56
0.8	12.22	4.28	122.42	0.35	1526.53	0.45
1.0	10.51	2.23	100.68	0.21	1078.73	0.37

Table 6 Magnetic data of $\text{Ni}_{0.2}\text{Mg}_{0.8}\text{Fe}_2\text{O}_4$ at various temperatures from M–H curves

Temperature (K)	M_s (emu/gm)	M_r (emu/gm)	H_c (Oe)
310	0.035	4.3	27.8
75	0.20	15	30.2
42	0.66	16.2	60.21
25	0.99	16.5	140.3
5	4.40	17	1200

that the ferric ions ($\sim 5 \mu\text{B}$) can be occupied by magnesium cations ($0 \mu\text{B}$) at B sites. As the ‘ x ’ value was increased, the ratio between ferric ions at B site and ferrous ions at A site will be reduced. This implied that the A–B super-exchange interaction was decreased [18]. Consequently, the M_s was decreased. In addition, the variation of M_s with composition of NMF is shown in Table 5. The H_c was decreased from 273.79 to 100.68 Oe with increase of Mg content. It would have occurred as a result of reduction in anisotropy constant (K) (see Table 5). This can normally allow the decreasing trend of the domain wall energy [38]. The numerical values of H_c , M_s , and K were computed using the standard relations mentioned in references [39–45] and further these values are listed in Table 5. Besides, the magnetic moment per formula unit ($\mu_B/\text{f.u.}$) was computed [40] and the values are listed in Table 5.

From Table 5, it was clear that magnetic moment values were decreased with increase in Mg content which in turn indicated the paramagnetic behavior of the ferrites. Furthermore, the variation of ‘ K ’ with Mg content is shown in Table 5. It can be understood that the ‘ K ’ value was decreased with increase in Mg content. Indeed, the M–H loops can be useful in evaluating the soft and hard kinds of magnetic specimen. This can be evidenced by means of the covered M–H loop area. That is, the large value of M–H loop area can predict the hard magnet nature while the small loop area can suggest the soft magnet nature of sample. However, the soft magnets can exhibit low coercive force. This

**Fig. 13** FC and ZFC curves of MgFe_2O_4 nanoparticles

was proved in the case of NMF system upon increasing the Mg content. That means, the soft magnetic behavior was increased upon increasing the dopant content. Therefore, these kinds of materials can be well suited for the transformers, inductor cores, recording heads, microwave devices, and magnetic shielding device applications.

3.5.2 FC and ZFC curves of MgFe_2O_4 and $\text{Ni}_{0.2}\text{Mg}_{0.8}\text{Fe}_2\text{O}_4$ nanoferrites

The magnetization curves of MgFe_2O_4 (MF) and $\text{Ni}_{0.2}\text{Mg}_{0.8}\text{Fe}_2\text{O}_4$ samples were recorded with varying magnetic field of $\pm 10 \text{ T}$ and the input temperature from 5 to 300 K. The ZFC and FC plots were drawn for MF and $\text{Ni}_{0.2}\text{Mg}_{0.8}\text{Fe}_2\text{O}_4$ at 10^2 Oe magnetic field. Figure 13 indicates the ZFC and FC curves of MF nanomaterial. It was clear from the ZFC and FC plots that at temperatures below 300 K, both the curves got separated into two different directions. Hence, above 300 K [blocking temperature (T_B)], the MF nanoparticles confirmed the SPM nature. It was also seen that the FC curve showed almost a constant manner

with reduction in temperature. This can be attributed to the uncoupled ferrite system. However, this uncoupled system was evidenced by agglomerated nanoparticles in the surface morphology. Thus, the particle to particle interaction may become high which can in turn stabilize the magnetic spins leading to almost constant trend of FC curve with temperature.

Figure 14 depicts the M–H loops of MF at 5 and 310 K taken over the input magnetic field of ± 10 T. It was obvious from the M–H loops recorded at 5 and 310 K that the SPM nature of the sample was spoiled with decrease of temperature. The high coercive force observed in the M–H curves (at 5 K) indicated the soft ferrite nature. However, at 300 K, the M–H loop expressed almost zero value of coercivity. It would have occurred as a result of exponential variation of fluctuation time associated with the particle moment with input temperature. Therefore, the magnetization seemed to switch quickly to a stable state with decrease of temperature. It had happened at T_B . It can basically depend linearly on the volume of material (V) and on the magnitude of ‘ K ’ [45].

The ZFC and FC plots of Ni_{0.2}Mg_{0.8}Fe₂O₄ at 100 Oe are depicted in Fig. 15. It was noted that the magnetization (M) was increased up to 45 K. Beyond 45 K, the M was decreased. In addition, M attained maximum value at 43 K. After crossing the 43 K temperature, the M started to decrease (as shown in inset plot of Fig. 15). This type of reduction in M will introduce the effective spin correlation between the spins or cluster in the ferrite system. Thus, it can lead to the reduction in M even at 100 Oe [33, 34].

The magnetization measurements of Ni_{0.2}Mg_{0.8}Fe₂O₄ were recorded over 5–310 K temperature at 100 Oe (input field). The plots were drawn between magnetization and applied magnetic field as shown in Fig. 16 at different low

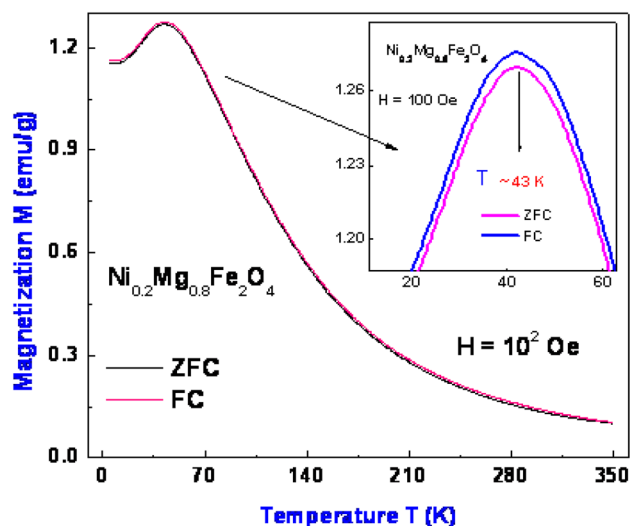


Fig. 15 FC and ZFC curves of Ni_{0.2}Mg_{0.8}Fe₂O₄ nanomaterials

temperatures such as 5, 42, 75 and 310 K. Among these plots, huge value of coercivity, about 1200 Oe at 5 K (see inset Fig. 16), was noted which in turn reflected the existence of SPM nanoparticles [36]. In general, this would have happened in the case of single-domain nanoparticles which can contain strong anisotropic forces. To magnetize the materials comprising of single-domain nanoparticles, huge amount of work must be done against the strong anisotropic forces. At this moment, the strong magnetic fields may be required and, therefore, it can possess high coercive force [41]. Besides, the M_r and H_c values of NMF ($x=0.8$) were evaluated at the four temperatures and listed in Table 6. It was obviously understood from Table 6 that huge value of coercivity

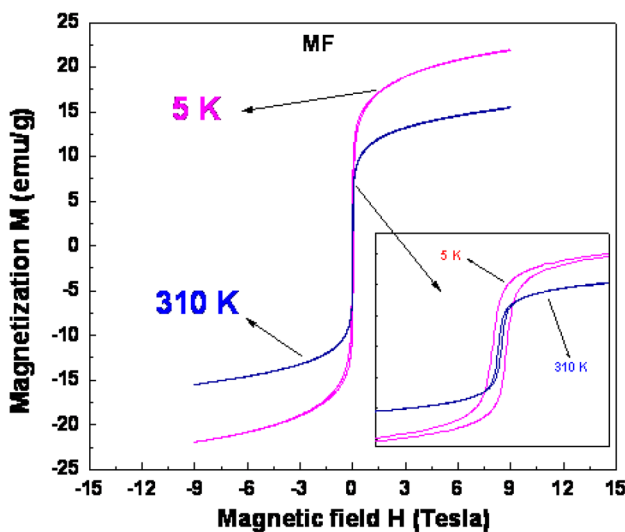


Fig. 14 M–H loops of MgFe₂O₄ (MF)

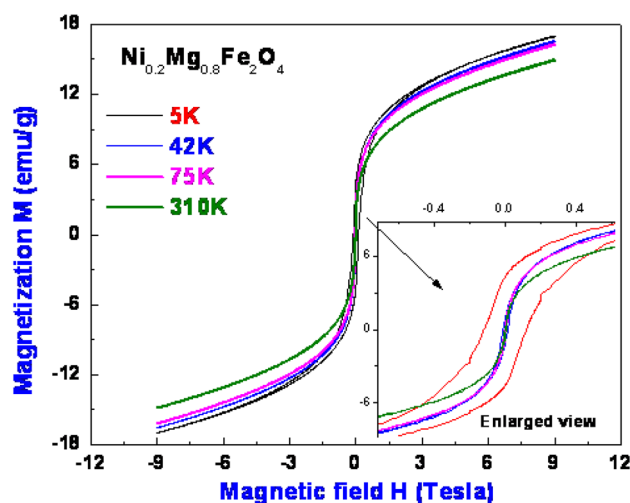


Fig. 16 M–H loops of Ni_{0.2}Mg_{0.8}Fe₂O₄ at various temperatures (at 100 Oe)

was noted at 5 K while an abrupt reduction in H_c and M_r was observed as a function of temperature (see Table 6). With increase of temperature, the H_c and M_r parameters were diminished gradually and approached almost equal to zero. This established the formation of SPM nanomaterials including the T_B . Hence, these kinds of nanoparticles can be used for biomedical applications such as magnetic resonance imaging (MRI).

3.6 Magnetic properties of $Ni_{1-x}Co_xFe_2O_4$ nanoferrite system

3.6.1 Room temperature magnetization measurements using VSM

Figure 17 revealed the M versus H loops (± 15 KOe) of NCF materials heated at 500 °C. The different magnetic parameters such as M_s , M_r , H_c and (M_r/M_s) were calculated to investigate the magnetic behavior. The results of magnetic parameters are reported in Table 7. It was understood from Fig. 17 and Table 7 that the M_s was increased upon increasing the cobalt concentration. However, the magnitude of M_s

was increased from ~17 to 34.4 emu/g (at room temperature) with increase of cobalt content in NCF system. It can be attributed to the increase of cobalt cations at nickel lattice site. In particular, the nickel cations with low magnetic moment of 3 μ_B were replaced by the cobalt cations containing high magnetic moment of 5 μ_B at the B sites. Moreover, the increasing trend of cobalt cations can in turn enhance the ratio of ferric and ferrous ions at B and A sites, respectively. Thus, the magnetic exchange interaction between the two sites will be increased [34]. Therefore, the M_s was increased. It was noticed that the H_c value was increased from 273.79 to 2342.33 Oe with increase of Co content. This established a fact that the huge amount of coercive field can be required to change magnetic moment thereby overcoming the anisotropic forces with increase of Co content. In this way, the ‘K’ value will be increased and, furthermore, it can increase the magnetic domain wall energy as reported in the published work [38]. As a matter of fact, the Co-doping into the nickel ferrite system supported the evolution of hard magnet nature owing to high coercivity value.

From Table 7, it was clear that magnetic moment values were increased with increase in Co content which can be attributed to the less probability for the occupancy of Co cations at octahedral sites. The data revealed that the increasing nature of cobalt content increased the magnetization and further the material was converted into hard magnetic material. It can be understood that the ‘K’ value was increased with increase of Co content. From the M–H loops of NCF, it was clear that the hard magnetic Ni–Co nanoferrites were prepared which can be magnetized and demagnetized hardly.

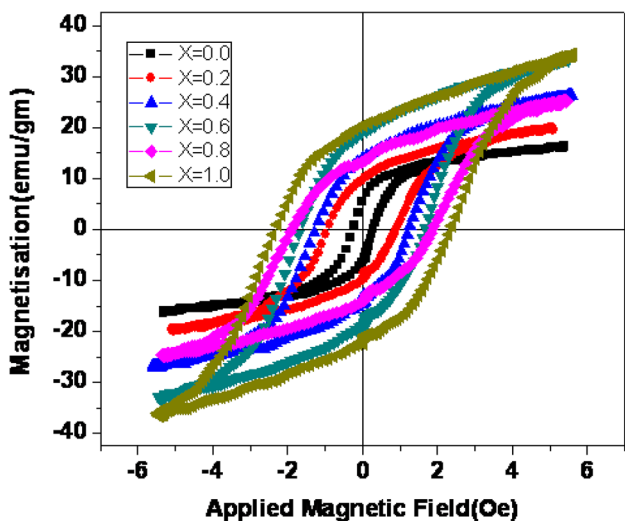


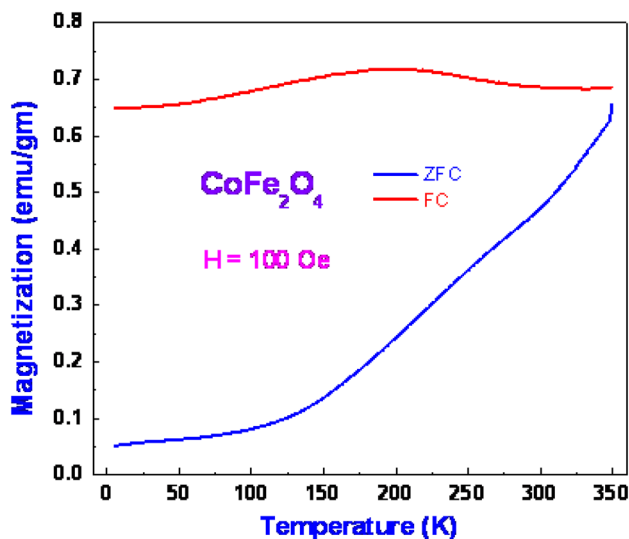
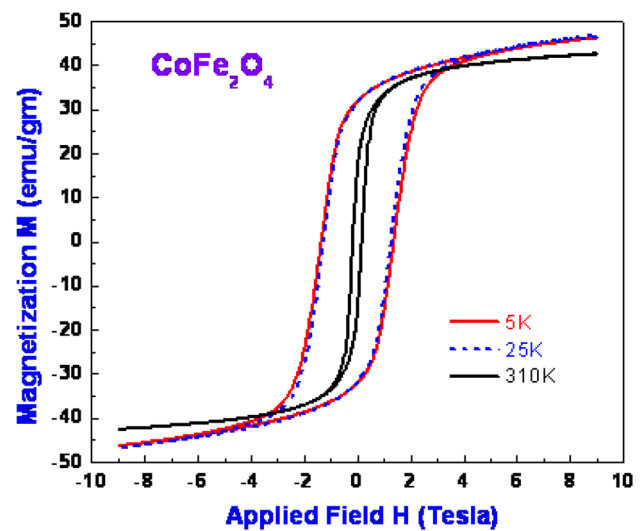
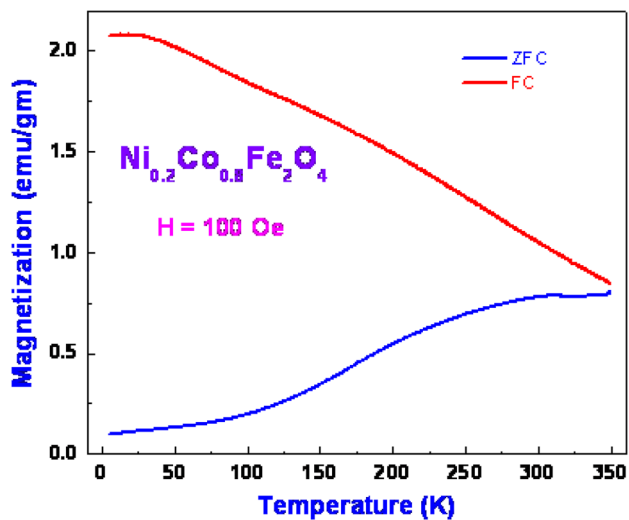
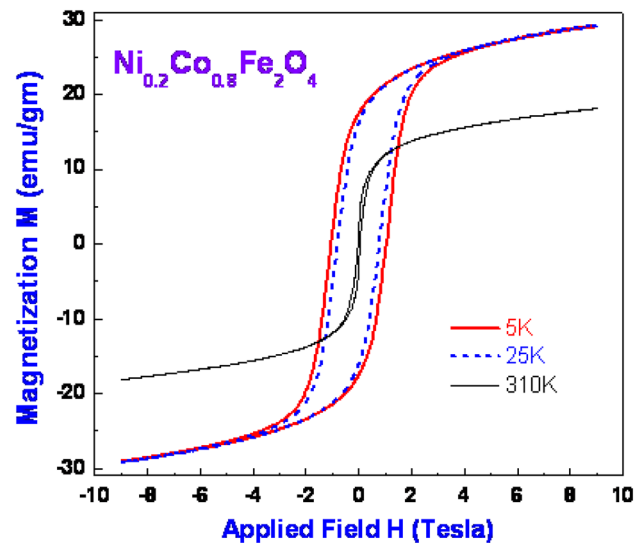
Fig. 17 M–H loops for all $Ni_{1-x}Co_xFe_2O_4$ nanoferrites ($x=0.0-1.0$)

3.6.2 FC and ZFC curves of $CoFe_2O_4$ and $Ni_{0.2}Co_{0.8}Fe_2O_4$ nanoferrites

The magnetization measurements of $CoFe_2O_4$ and $Ni_{0.2}Co_{0.8}Fe_2O_4$ nanomaterials were recorded with varying the applied magnetic field of ± 10 T at three different temperatures of 5, 25 and 310 K. Apart from these, the ZFC and FC plots were drawn (Figs. 18, 19) for the above-mentioned nanomaterials at 10^2 Oe. The usual behavior was observed in case of FC and ZFC curves of NCF. That is, the FC curves

Table 7 Data on M–H loops of $Ni_{1-x}Co_xFe_2O_4$ nanoferrites ($x=0.0-1.0$)

x	M_s (emu/gm)	M_r (emu/gm)	H_c (Oe)	M_r/M_s	K (erg/Oe)	Magnetic moment (μ_B)
0.0	16.450	6.535	273.790	0.39	4595.7	0.69
0.2	19.900	15.309	919.885	0.76	18,679.29	0.83
0.4	24.375	25.071	1251.15	0.94	31,119.16	1.02
0.6	26.411	25.874	1671.45	1.01	45,045.5	1.09
0.8	33.606	40.909	1876.057	1.20	64,333.44	1.41
1.0	34.360	41.360	2342.33	1.21	82,124.97	1.44


 Fig. 18 FC and ZFC curves of CoFe₂O₄ nanoparticles

 Fig. 20 M–H loops of CoFe₂O₄

 Fig. 19 FC and ZFC curves of Ni_{0.2}Co_{0.8}Fe₂O₄ nanoparticles

 Fig. 21 M–H loops of Ni_{0.2}Co_{0.8}Fe₂O₄

expressed almost a constant trend of M value while ZFC curves revealed the decreasing nature of M as a function of temperature. The similar observations were seen earlier in case of NMF nanomaterials. It was clear that the ZFC and FC curves of cobalt ferrite (CF) nanomaterials were merged at 355 K and below 355 K, both the curves were diverged (Fig. 18). This confirmed a fact that above 355 K, the CF nanomaterials acquired the SPM nature. However, this report established the $T_B \sim 355$ K. The diverging manner of ZFC and FC curves in general can indicate the ferromagnetic behavior of nanomaterials.

The ZFC and FC curves of Ni_{0.2}Co_{0.8}Fe₂O₄ nanoparticles are shown in Fig. 19. It was found that the T_B was ~ 353 K. Thus, the Ni_{0.2}Co_{0.8}Fe₂O₄ also exhibited the SPM nature

above T_B and below T_B ; the usual ferromagnetic behavior was noticed. In addition, the FC plot revealed the huge increase of magnetization as the temperature was decreased below T_B . This would have happened owing to the presence of uncoupled system in Ni_{0.2}Co_{0.8}Fe₂O₄.

Figures 20 and 21 depict the M–H loops of CF and Ni_{0.2}Co_{0.8}Fe₂O₄, respectively, at 5, 25 and 310 K of NCF system. It was obviously noticed from the M–H loops that the above-said two samples performed the ferrimagnetic behavior at all the temperatures. But nevertheless, the extent of ferrimagnetism was altered. Moreover, the magnetic parameters were calculated and are listed in Table 8. The M_s values of the CF and Ni_{0.2}Co_{0.8}Fe₂O₄ materials at 310 K were about

Table 8 Magnetic parameters for CoFe_2O_4 and $\text{Ni}_{0.2}\text{Co}_{0.8}\text{Fe}_2\text{O}_4$ nanoferrites at different temperatures 5, 25 and 340 K from hysteresis loops

Temperature (K)	CoFe_2O_4	$\text{Ni}_{0.2}\text{Co}_{0.8}\text{Fe}_2\text{O}_4$
H_c (Oe)		
310 K	1760	338
25 K	12,835	7822
5 K	13,600	10,364
M_s (emu/g)		
310 K	43	12
25 K	46	28
5 K	47	29
M_r (emu/g)		
310 K	16	2.4
25 K	32	16.6
5 K	33	17.4

43 and 12 emu/g, respectively. Herein, the saturation magnetization of CF was smaller than the published work for bulk CF [15]. From Table 8 and Figs. 20 and 21, it was noted that the H_c and M_s values were enhanced with increase of temperature. Specifically, the H_c of CF was increased from 1760 to 13,600 Oe. On the other hand, the $\text{Ni}_{0.2}\text{Co}_{0.8}\text{Fe}_2\text{O}_4$ showed the increasing value of the H_c from 338 to 10,364 Oe with decrease of temperature from 310 to 5 K. Moreover, the M_r was noticed to be increasing with decrease of temperature for all materials. As a whole, it was observed that at 310 K, the two nanomaterials showed soft ferrimagnetism in nature while for the rest of the temperatures, the sample revealed the hard magnetic nature. Therefore, at room temperature, these two samples may be used for transformer applications at high frequencies.

4 Conclusions

The NMF and NCF nanomaterials were prepared using citrate-gel method. The incorporation of magnesium ion into nickel ferrite system resulted in a decrease of crystallite size, saturation magnetization, coercivity and magnetic moment. The room temperature magnetization measurements indicated that NMF nano-ferrites showed narrow hysteresis loop with low saturation magnetization and low coercivity. This had happened due to the paramagnetic nature of the magnesium. Hence, these ferrites can be magnetically very soft materials. This kind of properties can be desirable for transformers, inductor cores, recording heads, microwave devices and magnetic shielding devices. The room temperature magnetization measurements of NCF revealed that the area in the hysteresis loop was more than NMF with moderate saturation magnetization and coercivity. This may be due

to the ferromagnetic nature of cobalt. Hence, these ferrites can reveal the hard magnetic nature. These characteristics of ferrites may be desirable for magnetic recording applications. Low-temperature magnetization measurements (M–H loops and FC and ZFC measurements) revealed that at low temperature, i.e., at 5 K, the materials were ferromagnetic in nature with high coercivity. The MgFe_2O_4 showed SPM behavior above room temperature. At 5 K temperature, the MF revealed large H_c of 1200 Oe suggesting the ferrimagnetic behavior. Beyond the T_B , the $\text{Ni}_{0.2}\text{Mg}_{0.8}\text{Fe}_2\text{O}_4$ nanomaterials showed anhysteresis curve and less than T_B , it exhibited the lagging nature of M behind H and further suggested SPM behavior of nanomaterials. Therefore, the $\text{Ni}_{0.2}\text{Mg}_{0.8}\text{Fe}_2\text{O}_4$ nanoparticles can provide biomedical applications in drug delivery and in MRI. Low-temperature magnetization measurements (M–H loops and FC and ZFC measurements) revealed that below room temperature, i.e., at 5 and 25 K, the materials were ferromagnetic in nature with high coercivity. CoFe_2O_4 and CoFe_2O_4 nanoferrites showed SPM behavior above room temperature (at around 355 K) where coercivity and remanence became zero. Above blocking temperature, CoFe_2O_4 and $\text{Ni}_{0.2}\text{Co}_{0.8}\text{Fe}_2\text{O}_4$ nanoferrites showed anhysteresis and below T_B , they showed large hysteresis which can be the criteria of a superparamagnetic behavior. Inclusion of Co in nickel ferrite decreased the coercivity from 1760 to 338 Oe at room temperature by making the material magnetically very soft favoring its application in high-frequency transformers.

Acknowledgements The authors (AG and DR) are very grateful to Prof. G. Prasad, Head, Department of Physics, Osmania University, Hyderabad, and also thankful to UPE-UGC-OU and DST-PURSE-OU. Authors K. M. Batoo, S. F. Adil and M. Khan are thankful to the Deanship of Scientific Research at King Saud University for its funding through the Research Group Project no. RG-1437-030.

References

1. N. Boda, K.C.B. Naidu, K.M. Batoo, G.H.R. Joice, J.L. Naik, D. Ravinder, Structural, morphological and electronic properties of cadmium cobalt ferrite nanoparticles. *Biointerface Res Appl Chem* **10**, 4752–4763 (2020)
2. U. Naresh, R.J. Kumar, K.C.B. Naidu, Optical, magnetic and ferroelectric properties of $\text{Ba}_{0.2}\text{Cu}_{0.8-x}\text{La}_x\text{Fe}_2\text{O}_4$ ($x=0.2-0.6$) nanoparticles. *Ceram Int* **45**, 7515–7523 (2019)
3. K.K. Kefeni, B.B. Mamba, T.A.M. Msagati, Application of spinel ferrite nanoparticles in water and waste water treatment: a review. *Sep Purif Technol* **188**, 399–422 (2017)
4. N. Boda, G. Boda, K.C.B. Naidu, M. Srinivas, K.M. Batoo, D. Ravinder, A.P. Reddy, Effect of rare earth elements on low temperature magnetic properties of Ni and Co-ferrite nanoparticles. *J Magn Magn Mater* **473**, 228–235 (2019)
5. K.C.B. Naidu, N.S. Kumar, G.R. Kumar et al., Temperature and frequency dependence of complex impedance parameters of microwave sintered NiMg ferrites. *J Aust Ceram Soc* **55**, 541–548 (2019)

6. D. Sivakumar, K.C.B. Naidu, K.P. Nazeer, M.M. Rafi, G. Rameshkumar, B. Sathyaseelan, G. Killivalavan, A.A. Begam, Structural characterization and dielectric properties of superparamagnetic iron oxide nanoparticles. *J Korean Ceram Soc* **55**, 230–238 (2018)
7. D.S. Kumar, K.C.B. Naidu, M.M. Rafi, K.P. Nazeer, A.A. Begam, G.R. Kumar, Structural and dielectric properties of superparamagnetic iron oxide nanoparticles (SPIONs) stabilized by sugar solutions. *Mater Sci Pol* **36**, 123–133 (2018)
8. N.R. Ram, M. Prakash, U. Naresh, N.S. Kumar, T.S. Sarmash, T. Subbarao, R.J. Kumar, G.R. Kumar, K.C.B. Naidu, Review on magnetocaloric effect and materials. *J Supercond Nov Magn* **31**, 1971–1979 (2018)
9. T. Ramaprasad, R.J. Kumar, U. Naresh, M. Prakash, D. Kothandan, K.C.B. Naidu, Effect of pH value on structural and magnetic properties of CuFe₂O₄ nanoparticles synthesized by low temperature hydrothermal technique. *Mater Res Express* **5**, 095025 (2018)
10. D. Kumar, D.B. Das, R. Gopalan, Effects of surfactant on the structural and magnetic properties of hydrothermally synthesized NiFe₂O₄ nanoparticles. *Mater Chem Phys* **218**, 70–76 (2018)
11. B. Aslibeiki, G. Varvaro, D. Peddis, P. Kameli, Particle size, spin wave and surface effects on magnetic properties of MgFe₂O₄ nanoparticles. *J Magn Magn Mater* **422**, 7–12 (2017)
12. N. Kaur, M. Kaur, Envisioning the composition effect on structural, magnetic, thermal and optical properties of mesoporous MgFe₂O₄-GO nanocomposites. *Ceram Int* **44**, 4158–4168 (2018)
13. R. Lamouri, O. Mounkachi, E. Salmani, M. Hamedoun, A. Benyoussef, H. Ez-Zahrouy, Size effect on the magnetic properties of CoFe₂O₄ nanoparticles: a Monte Carlo study. *Ceram Int* (2019). <https://doi.org/10.1016/j.ceramint.2019.12.035>
14. S. Munjal, N. Khare, B. Sivakumar, D.N. Sakthikumar, Citric acid coated CoFe₂O₄ nanoparticles transformed through rapid mechanochemical ligand exchange for efficient magnetic hyperthermia applications. *J Magn Magn Mater* **477**, 388–395 (2019)
15. D. Hu, F. Zhao, Z. Zhang, L. Miao, R. Ma, W. Zhao et al., Synthesis and magnetic properties of monodisperse CoFe₂O₄ nanoparticles coated by SiO₂. *Ceram Int* **44**, 22462–22466 (2018)
16. S. Ramesh, D. Ravinder, K.C.B. Naidu, N.S. Kumar, K. Srinivas, D.B. Basha, B.C. Sekhar, A review on giant piezoelectric coefficient, materials and applications. *Biointerface Res Appl Chem* **9**, 4205–4216 (2019)
17. N. Boda, K.C.B. Naidu, D.B. Basha, D. Ravinder, Structural and magnetic properties of CdCoFe₂O₄ nanoparticles. *J. Supercond. Nov. Magn.* 1–6 (2019). <https://doi.org/10.1007/s10948-019-05242-1>
18. K.C.B. Naidu, W. Madhuri, Microwave processed NiMg ferrites: studies on structural and magnetic properties. *J Magn Magn Mater* **420**, 109–116 (2016)
19. K.C.B. Naidu, W. Madhuri, Ceramic nanoparticle synthesis at lower temperatures for LTCC and MMIC technology. *IEEE Trans Magn* **54**, 2300808 (2018). <https://doi.org/10.1109/TMAG.2018.2855663>
20. M. Hashim, K.C.B. Naidu, G.H.R. Joice, J.L. Naik, D. Ravinder, Superparamagnetic and photocatalytic activity of CoCe_{0.02}Dy_{0.02}Fe_{1.96}O₄ nanoparticles synthesized by citrate-gel autocombustion technique. *Biointerface Res Appl Chem* **9**, 4164–4167 (2019)
21. C.H. Vinutha, K.C.B. Naidu, C.C. Sekhar, D. Ravinder, Magnetic and antimicrobial properties of cobalt zinc ferrite nanoparticles synthesized by citrate-gel method. *Int J Appl Ceram Technol* **16**, 1944 (2019). <https://doi.org/10.1111/ijac.13276>
22. S. Joshi, M. Kumar, Effect of Ni²⁺ substitution on structural, magnetic, dielectric and optical properties of mixed spinel CoFe₂O₄ nanoparticles. *Ceram Int* **42**, 18154–18165 (2018)
23. G. Aravind, M. Raghasudha, D. Ravinder, M.M. Raja, S.S. Meena, P. Bhatt, M. Hashim, Study of structural and magnetic properties of Li–Ni nanoferrites synthesized by citrate-gel auto combustion method. *Ceram Int* **42**, 2941–2950 (2016)
24. M. Hashim, M. Raghasudha, J. Shah, S.E. Shirsath, D. Ravinder, S. Kumar, S.S. Meena, P. Bhatt, R. Kumar, R.K. Kotnala, High temperature dielectric studies of indium-substituted NiCuZn nanoferrites. *J Phys Chem Solids* **112**, 29–36 (2018)
25. F.R. Mariosi, J. Venturini, A. da Cas Viegas, C.P. Bergmann, Lanthanum-doped spinel cobalt ferrite (CoFe₂O₄) nanoparticles for environmental applications. *Ceram Int* (2019). <https://doi.org/10.1016/j.ceramint.2019.09.266>
26. P. Scherrer, Bestimmung der Grosse und der Inneren Struktur von Kolloidteilchen Mittels Rontgenstrahlen, *Nachrichten von der Gesellschaft der Wissenschaften, Gottingen. Math-Phys Kl* **2**, 98–100 (1918)
27. N.S. Kumar, R.P. Suvarna, K.C.B. Naidu, Grain and grain boundary conduction mechanism in sol-gel synthesized and microwave heated Pb_{0.8-y}La_yCo_{0.2}TiO₃ (y = 0.2–0.8) nanofibers. *Mater Chem Phys* **223**, 241–248 (2019)
28. A.R. Denton, N.W. Ashcroft, Vegard's law. *Phys Rev A* **43**, 3161 (1991)
29. R.D. Shannon, Revised effective ionic radii and systematic studies of interatomic distances in halides and chalcogenides. *Acta Cryst A* **32**, 751–767 (1976)
30. N.S. Kumar, R.P. Suvarna, K.C.B. Naidu, G.R. Kumar, S. Ramesh, Structural and functional properties of sol-gel synthesized and microwave heated Pb_{0.8}Co_{0.2-z}La_zTiO₃ (z = 0.05–0.2) nanoparticles. *Ceram Int* **44**, 19408–19420 (2018)
31. N.S. Kumar, R.P. Suvarna, K.C.B. Naidu, Sol-gel synthesized and microwave heated Pb_{0.8-y}La_yCo_{0.2}TiO₃ (y = 0.2–0.8) nanoparticles: structural, morphological and dielectric properties. *Ceram Int* **44**, 18189–18199 (2018)
32. D. Kothandan, R.J. Kumar, M. Prakash, K.C.B. Naidu, Structural, morphological and optical properties of Ba_{1-x}Cu_xTiO₃ (x = 0.2, 0.4, 0.6, 0.8) nanoparticles synthesized by hydrothermal method. *Mater Chem Phys* **215**, 310–315 (2018)
33. R. Chantrell, N.S. Walmsley, J. Gore, M. Maylin, Theoretical studies of the field-cooled and zero-field cooled magnetization of interacting fine particles. *J Appl Phys* **85**, 4340 (1999)
34. U. Naresh, R.J. Kumar, K.C.B. Naidu, Hydrothermal synthesis of barium copper ferrite nanoparticles: nanofiber formation, optical, and magnetic properties. *Mater Chem Phys* **236**, 121807 (2019)
35. L.J. Berchmens, R.K. Selvan, P.N.S. Kumar, C.O. Augustin, Structural and electrical properties of Ni_{1-x}Mg_xFe₂O₄ synthesized by citrate gel process. *J Magn Magn Mater* **279**, 103–110 (2004)
36. S.R. Shinde, S.D. Kulkarni, A.G. Banpurkar, R. Nawathey-Dixit, S.K. Date, S.B. Ogale, Magnetic properties of nanosized powders of magnetic oxides synthesized by pulsed laser ablation. *J Appl Phys* **88**, 1566 (2000)
37. M.A. Gabal, Y.M. AlAngari, H.M. Zaki, Structural, magnetic and electrical characterization of Mg–Ni nanocrystalline ferrites prepared through egg white precursor. *J Magn Magn Mater* **363**, 6–15 (2014)
38. E.C. Stoner, E.P. Wohlfarth, A mechanism of magnetic hysteresis in heterogeneous alloys. *Phil Trans R Soc Lond A* **240**, 599 (1948)
39. C.P. Bean, J.D. Livingston, Superparamagnetism. *J Appl Phys* **30**, 120 (1959)
40. N. Raghuram, T.S. Rao, K.C.B. Naidu, Magnetic properties of hydrothermally synthesized Ba_{1-x}Sr_xFe₁₂O₁₉ (x = 0.0–0.8) nanomaterials. *Appl Phys A* **125**, 839 (2019)
41. U. Naresh, R.J. Kumar, K.C.B. Naidu, Structural, morphological, optical, magnetic and ferroelectric properties of Ba_{0.2}La_{0.8}Fe₂O₄ nanofibers. *Biointerface Res Appl Chem* **9**, 4243–4247 (2019)
42. D.R. Mane, D.D. Birajdar, S.E. Shirsath, R.A. Telugu, R.H. Kadam, Structural and magnetic characterizations of Mn–Ni–Zn ferrite nanoparticles. *Phys Status Solidi A* **207**, 2355 (2010)

43. S. Singhal, K. Chanda, Cation distribution and magnetic properties in chromium-substituted nickel ferrites prepared using aerosol route. *J Solid State Chem* **180**, 296 (2007)
44. C.M. Hurd, Varieties of magnetic order in solids. *Contemp Phys* **23**, 469 (1982)
45. D.J. Craik, *Magnetic oxides, part II* (Wiley, London, 1975), p. 703

Publisher's Note Springer Nature remains neutral with regard to jurisdictional claims in published maps and institutional affiliations.